Free PCR virus detection via few-layer bismuthene and tetrahedral DNA nanostructured assemblies

Laura Gutiérrez-Gálvez [a], Daniel García-Fernández [a], Melisa del Barrio [a,1], Mónica Luna [b], Íñigo Torres [c,d], Félix Zamora [c,d], Cristina Navío [e], Paula Milán-Rois [e], Milagros Castellanos [e], Melanie Abreu [f], Rafael Cantón [g], Juan Carlos Galán [f,h], Álvaro Somoza [e], Rodolfo Miranda [e], Tania García-Mendiola [a,d,*], Encarnación Lorenzo [a,d,e]

[a] Departamento de Química Analítica y Análisis Instrumental, Universidad Autónoma de Madrid (UAM), 28049, Madrid, Spain
[b] Instituto de Micro y Nanotecnología IMN-CNM, CSIC (CEI UAM+CSIC), 28760, Tres Cantos, Madrid, Spain
[c] Departamento de Química Inorgánica and Condensed Matter Physics Center (IFIMAC), Universidad Autónoma de Madrid, 28049, Madrid, Spain
[d] Institute for Advanced Research in Chemical Sciences (IAdChem), Universidad Autónoma de Madrid, 28049, Madrid, Spain
[e] IMDEA-Nanociencia, Ciudad Universitaria de Cantoblanco, 28049, Madrid, Spain
[f] Servicio de Microbiología, Hospital Universitario Ramón y Cajal and Instituto Ramón y Cajal de Investigación Sanitaria (IRYCIS), 28034, Madrid, Spain
[g] CIBER de Enfermedades Infecciosas (CIBERINFEC), Instituto de Salud Carlos III, Madrid, Spain
[h] Centro de Investigación Biomédica en Red en Epidemiología y Salud Pública (CIBERESP), Madrid, Spain

A B S T R A C T

In this work we describe a highly sensitive method based on a biocatalyzed electrochemiluminescence approach. The system combines, for the first time, the use of few-layer bismuthene (FLB) as a platform for the oriented immobilization of tetrahedral DNA nanostructures (TDNs) specifically designed and synthetized to detect a specific SARS-CoV-2 gene sequence. In one of its vertices, these TDNs contain a DNA capture probe of the open reading frame 1 ab (ORF1ab) of the virus, available for the biorecognition of the target DNA/RNA. At the other three vertices, there are thiol groups that enable the stable anchoring/binding to the FLB surface. This novel geometry/approach enables not only the binding of the TDNs to surfaces, but also the orientation of the capture probe in a direction normal to the bismuthine surface so that it is readily accessible for binding/recognition of the specific SARS-CoV-2 sequence. The analytical signal is based on the anodic electrochemiluminescence (ECL) intensity of luminol which, in turn, arises as a result of the reaction with H_2O_2, generated by the enzymatic reaction of glucose oxidation, catalyzed by the biocatalytic label avidin-glucose oxidase conjugate (Av-GOx), which acts as co-reactant in the electrochemiluminescent reaction. The method exhibits a limit of detection (LOD) of 4.31 aM and a wide linear range from 14.4 aM to 1.00 μM, and its applicability was confirmed by detecting SARS-CoV-2 in nasopharyngeal samples from COVID-19 patients without the need of any amplification process.

Author contributions

Laura Gutiérrez Gálvez and Daniel García Fernández have prepared DNA nanostructures. Laura Gutiérrez Gálvez, Melisa del Barrio and Daniel García Fernández have carried out the experiments regarding the biosensor development. Mónica Luna has performed the AFM, SEM and Fluorescence Microscopy characterization. Iñigo Torres has synthetized and characterized the few layers of bismuthene. Félix Zamora has supervised the experimental results regarding the few layers of bismuthene preparation. Cristina Navio has carried out the experiments related to XPS. Tania García-Mendiola, and Encarnación Lorenzo have supervised the experimental results regarding the biosensor. Laura Gutiérrez Gálvez, Tania García-Mendiola and Encarnación Lorenzo have elaborated the manuscript. Melanie Abreu, Rafael Cantón and Juan Carlos Galán have obtained the samples from patients and performed the qPCR. Paula Milán-Rois and Milagros Castellanos have extracted and

quantified the viral RNA from patient's samples. Álvaro Somoza and Rodolfo Miranda have supervised experimental results regarding RNA samples and review & editing the manuscript.

1. Introduction

Thus far, in the 21st century, there have been three human pathogenic coronavirus outbreaks: SARS-CoV (2003), MERS-CoV (2012), and SARS-CoV-2 (2019) [1]. The most recent outbreak led to the Coronavirus Disease 2019 (COVID-19) pandemic that has, and continues to, dramatically challenge public health and economic systems worldwide [2].

During the early stages of the COVID-19 outbreak, several cases of infected patients were not correctly diagnosed due to the lack of efficient and specific diagnostic tools that could discriminate between common flu and COVID-19 symptoms [3]. Since then, new approaches for early diagnosis and monitoring of COVID-19 have and continue to be developed [4]. Current methods include quantitative reverse transcription polymerase chain reaction (RT-qPCR), antigen or serological tests. For the general population, the most accessible tool is the antigen test, which directly detects viral proteins related to the virus in nasal or oropharyngeal samples in an easy and rapid form, which can even be used at home. However, this test can be up to 10^5 times less sensitive than the "gold standard" RT-qPCR system [5]. Other systems include serological tests, which qualitatively or quantitatively measure the antibody response to SARS-CoV-2 infection or vaccination. Clinically, the qualitative assay allows rapid detection of a current and/or past infection, depending on when the sample is taken after viral exposure. Hence, these serological tests serve as complementary methodologies to the RT-qPCR; the standard diagnosis that allows the detection with high sensitivity and accuracy of viral nucleic acid usually extracted from nasopharyngeal/oropharyngeal swabs [5]. This methodology has been officially approved by the World Health Organization (WHO) as a standardized method for diagnosing COVID-19 [6]. However, this approach presents some drawbacks, including laboriousness, long processing time, and the need for specialized instruments and skilled personnel. These limitations have encouraged efforts to develop alternative diagnosis systems [7,8]. In this context, biosensors have emerged and can be considered as one of the most powerful alternatives because they can easily overcome the shortcomings mentioned above. This is due to their high sensitivity and selectivity, short response time, cost-effectiveness, ease of fabrication and use, adaptable nature, and the possibility of miniaturization [9]. As a result, new approaches, based on new configurations and the combination of different types of nanomaterials, for the detection of the genetic material of SARS-CoV-2 have been recently reported [10–15].

In most of the reported systems, immobilization of the DNA capture probe on the transducer is carried out by the traditional two-step assembly strategy consisting of the chemisorption of the thiolated single-stranded DNA probe on the surface of the gold, followed by a passivation step with an alkanethiol, such as mercaptohexanol (MCH). This second step is required to fill out the remaining space on the gold surface to favor the perpendicular orientation of the DNA strands, which is critical to enable the hybridization with the target nucleic acid [16]. However, new DNA immobilization methodologies, geometries and platforms are needed to improve control of probe-probe and probe-analyte interactions on surfaces due to the reduced mass transport and the presence of crowding effects that occur under these conditions when compared to probe-analyte recognition in homogeneous solution [17]. For this reason, numerous approaches have been pursued to improve event recognition in heterogeneous systems based on surface-bound probes. In particular, DNA technology has emerged as a novel approach to achieve improved probe-analyte recognition by introducing 3D DNA nanostructures as biorecognition elements instead

of single-stranded DNAs. Specifically, tetrahedral DNA nanostructures (TDNs) have attracted a great deal of interest in the scientific community for their simple synthesis [11], mechanical rigidity, and structural stability [18]. In addition, many authors have reported on the advantages of TDNs-based DNA biosensors, including reduced background signals, improved hybridization efficiency, fewer non-specific adsorptions, and significantly improved detection sensitivity [19]. In the present work, we have employed new tetrahedral DNA nanostructures as capture probes specifically designed to recognize a DNA sequence of SARS-CoV-2 efficiently and selectively.

The development and use of two-dimensional (2D) nanomaterials is an area that has experienced an explosive growth in recent years. This has, in turn, stimulated and attracted, and continues to attract, attention and application in a wide range of areas. Of particular note and relevance in the context of sensors and biosensors, such efforts have contributed to significant advances in the biosensing landscape and to the development of sophisticated, smart, and miniaturized devices [20]. Therefore, significant research should be conducted in this emerging and exciting field of study. Among these 2D nanomaterials, bismuthene is one of the most recently identified 2D nanomaterials, and its use for sensing and other applications is just emerging. Monolayer and few-layer 2D bismuth(ene) [21], has been the subject of recent work [20,22–25] due to its outstanding metallic properties, chemical and thermal stability, excellent biocompatibility and strong light–material interactions [22]. These attractive properties have stimulated the use of this emerging material in biosensing technologies/applications [26]. In addition, bismuthene offers the possibility of being used as an immobilization platform of thiolated biorecognition elements via its strong interactions with thiol groups [27–30]. Despite its potential in the sensing field, the application of bismuthene in biosensor development remains challenging and little explored.

Among the various transduction modes in biosensors, electrochemiluminescence (ECL) has been gaining importance in recent times because of its high sensitivity, wide detection range, fast response, simple equipment, and low cost [31]. These attributes make ECL especially attractive, mainly when compared to conventional approaches, for the development of highly efficient, sensitive, and precise detection of analytes at trace levels in the clinical area for early diagnosis of diseases [32].

With the intent of developing highly sensitive and selective Covid biosensors, we have designed and synthesized tetrahedral DNA nanostructures, designed to recognize a specific SARS-CoV-2 gene sequence and have combined them with few-layer bismuthene for the development of a very sensitive ECL-based biosensor. An amplified signal response is obtained with a glucose oxidase reporter probe through the generation of H_2O_2, which acts as a co-reactant with luminol, generating an enhanced biocatalyzed ECL response. This biocatalyzed ECL system exhibited a limit of detection (LOD) of 4.31 aM and an exceptionally wide linear range response from 14.4 aM to 1.00 μM. It has been successfully applied to the detection of SARS-CoV-2 ORF1ab gene in nasopharyngeal samples of infected patients.

2. Material and methods

All chemicals and instrumentation used are described in the Supporting Information (SI).

2.1. Procedures

2.1.1. Optimized synthesis of tetrahedral DNA nanostructures

The four oligonucleotides (Tetra-A/Tetra-A-ORF/Tetra-A-ORF-FAM, Tetra-B, Tetra-C and Tetra-D; listed in Table S1) were mixed in equimolar quantities in TM buffer (20 mM Tris 50 mM $MgCl_2$ pH 8.0). Then, the mixture was subjected in a thermocycler to a treatment based on

three different stages divided into steps of 2 min each. Specifically, the first stage consists of 2 different steps at 95 °C and 51 °C; the second one of 4 steps at 46.1 °C, 43.6 °C, 41.2 °C and 38.8 °C; and the last one of 2 steps of 30 °C and 4 °C.

2.1.2. SARS-CoV-2 nasopharyngeal samples from patients

RNA from inactivated swab nasopharyngeal samples obtained from COVID-19 patients and donated by Hospital Ramón y Cajal (Madrid) was extracted with the QIAamp Viral RNA Qiagen kit. The total RNA obtained was eluted in water free of RNase, and its concentration was measured using a Nanodrop prior to its storage at – 80 °C. To avoid any cross-contamination between samples and/or during their manipulation by the operator, all procedures were performed in P2-biosecurity cabinets with spatial and temporal separation between COVID-19 positive and negative samples. Two positive samples with different viral load (cycle threshold values (Cts) of 15 (patient 3, P3), 20 (patient 2, P2), and 29 (patient 1, P1)) and negative samples (5 samples with a Cts value above the threshold ~35) were analyzed by RT-qPCR. These samples were also analyzed with the developed biosensor after 1:10 dilution in sterilized purified Milli-Q water. The samples were obtained with the consent of all participants and approved by "Comité de Ética de la Investigación con Medicamentos del Hospital Universitario Ramón y Cajal". Reference: 127–21.

2.1.3. Biosensor development and SARS-CoV-2 ORF1ab gene detection

CSPEs were first nanostructured by drop-casting 10.0 µL of FLB dispersion (1.0 mg/mL) in isopropanol previously vortexed to avoid aggregation and ensure the homogeneity of the dispersion [23]. To allow the fast evaporation of the solvent, the electrodes were heated at 75 °C on a hot plate during the process. Then, the electrodes were allowed to cool to room temperature. Afterward, the nanostructured electrodes (CSPE/FLB) were incubated overnight with 10.0 µL of 1.00 µM tetrahedral DNA nanostructure, which carries SARS-CoV-2 ORF1ab gene capture probe in one of its vertices (TDN-ORF). A washing step was carried out to remove non-absorbed materials by immersing the modified electrodes (CSPE/FLB/TDN-ORF) for 10 min in sterilized purified Milli-Q water. Then, electrodes were incubated in a humid chamber for 1 h at 37 °C with 10.0 µL of the analyte (ORF-C) with appropriate concentration and submitted to another washing step as previously described. Subsequently, the electrodes (CSPE/FLB/TDN-ORF/ORF-C) were further incubated in a humid chamber for 30 min at 37 °C with 10.0 µL of a biotinylated reported probe (Probe-2-Biotin) in a concentration of 1.00 µM. After another washing step, the electrodes (CSPE/FLB/TDN-ORF/ORF-C/Probe-2-Biotin) were finally exposed to 6.00 µL of 25 µg/mL Av-GOx for 35 min, followed by another washing step to obtain the final platform CSPE/FLB/TDN-ORF/ORF-C/Probe-2-Biotin/Av-GOx. Then, the prepared electrodes were incubated at room temperature with 25.0 µL of 30 mM glucose in 10 mM PB pH 7 for 30 min to generate hydrogen peroxide

(H_2O_2). Afterward, 0.1 M NaOH was added to reach pH 9 to obtain high luminol ECL signal. Finally, luminol in 0.2 M PB pH 9 was added to reach a final concentration of 50 µM and ECL signal was immediately generated by applying a cyclic potential scan from 0.00 V to 1.40 V at a scan rate of 100 mV/s. The ECL signal and cyclic voltammogram were registered simultaneously.

2.1.4. Detection of SARS-CoV-2 ORF1ab gene in nasopharyngeal samples

5.00 µL of the nasopharyngeal sample (see 1.1.2. section of SI) were incubated in a humid chamber (1 h at 37 °C) onto the designed platform (CSPE/FLB/TDN-ORF) and washed by immersion in sterilized purified Milli-Q water for 10 min. Next steps (hybridization with Probe-2-Biotin, immobilization of Av-GOx, and electrochemiluminescence detection of SARS-CoV-2 ORF1ab gene) were performed as described in 2.1.2. section.

3. Results and discussion

3.1. Biosensor design

The proposed biosensor design is depicted in Scheme 1 and is based on 7 basic steps. In the first step, CSPEs were modified with FLB (CSPE/FLB) by direct adsorption, as described in the material and methods section. Upon this nanostructured surface, the tetrahedral DNA nanostructures, which carry the ORF1ab gene capture probe (TDN-ORF) were immobilized by chemisorption onto the FLB through the three thiol groups present at the basal vertices of the TDN (step 2). The obtained platform (CSPE/FLB/TDN-ORF) was then challenged with target DNA (step 3), the SARS-CoV-2 ORF1ab gene sequence, which is 28 nucleotides long (CSPE/FLB/TDN-ORF/ORF-C). As the ORF1ab capture probe in the TDN-ORF contains only 14 nucleotides, the analyte keeps 14 nucleotides free for a second hybridization with a biotin-tagged reporter probe (ORF-2-Biotin), obtaining the platform CSPE/FLB/TDN-ORF/ORF-C/ORF-2-Biotin (step 4). The biotinylated probe allows the subsequent immobilization of the biocatalytic label (the avidin-glucose oxidase conjugate (Av-GOx)) (step 5). The ECL signal of the CSPE/FLB/TDN-ORF/ORF-C/ORF-2-Biotin/Av-GOx platform is registered in the presence of luminol and H_2O_2, which is generated by the enzymatic reaction that takes place during the incubation with glucose (steps 6 and 7). There is not ECL signal of luminol in absence of H_2O_2, which acts as co-reactant (Fig. S1). However, in presence of H_2O_2 the luminol signal increases on increasing the concentration of H_2O_2.

3.2. Few-layer bismuthene synthesis and characterization

Firstly, FLB was prepared on a two-step procedure under mild conditions [23] (see SI). The FLB hexagons were characterized in-depth morphologically and spectroscopically. Transmission Electron
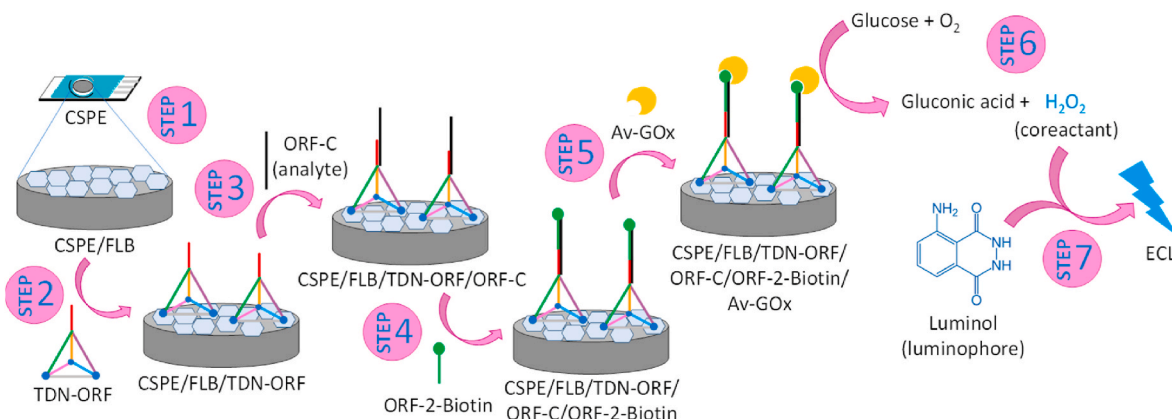
Scheme 1. TDN and FLB-based biocatalyzed ECL biosensor for SARS-CoV-2 ORF1ab gene detection.

Microscopy (TEM) images revealed the hexagonal morphology and the over-micron lateral dimensions (Fig. 1A and S2). The morphology and size were also confirmed by Scanning Electron Microscopy (SEM) (Fig. 1B and S3). Additionally, Atomic Force Microscopy (AFM) was used to verify the morphology and evaluate the lateral sizes and thickness of the FLB (Fig. 1C). Statistical analysis using AFM images (Fig. S4) revealed that most of the FLB hexagons present thicknesses below 20 nm, lateral dimensions over 2 μm, and areas around 4–10 μm^2 (Fig. S5). The structure of the FLB hexagons was also evaluated with X-ray powder diffraction (XRPD) spectroscopy, revealing the bismuth rhombohedral β-phase structure (PDF: 04-006-7762) (Fig. 1D). Furthermore, the FLB nanosheets were analyzed by Raman spectroscopy. Thus, while bulk bismuth exhibits two main phonon peaks, E_g and A_{1g} modes at 71 cm^{-1} and 98 cm^{-1}, respectively [33], the single point Raman spectrum of an FLB hexagon of 5 nm thickness displays a blue shift of these bands, showing the E_g mode at 83.3 cm^{-1} and the A_{1g} mode at 106.6 cm^{-1} (Fig. 1E). This observation agrees with the thickness dependence of antimonene previously reported [34,35]. The Raman spatial mapping generated by the A_{1g} mode showed the same hexagonal morphology observed by the other microscopy techniques (Fig. 1F). Hence, the crystallinity and 2D aspect ratio point out the high quality of the FLB hexagons.

3.3. Tetrahedral DNA nanostructure synthesis optimization and characterization

The TDN was prepared by using three thiolated DNA 55-base long oligonucleotides (Tetra-B, Tetra-C, and Tetra-D) and a fourth 80-nucleotide strand (Tetra-A-ORF) that contains the DNA capture probe. Here, we report the use of a DNA capture probe complementary to a specific SARS-CoV-2 gene region coding for the ORF1ab gene at its 5′ end. According to this design, each oligonucleotide forms one of the 4 faces of the tetrahedron (Fig. 2A). Each of them has a fragment of 17 base pairs complementary to each of the other three oligonucleotides. The

complementary zones between them are indicated with the same color in Fig. 2A and Table S1. The TDN has the ORF1ab capture probe at one vertice (TDN-ORF), exposed to the solution and ready to hybridize with the target DNA, and three thiol groups at the basal vertices to be anchored to the FLB.

There are some procedures for TDN synthesis reported in the literature [17,36–40], however, they do not pay attention to the possibility of obtaining random structures. In this sense, we designed an improved synthesis method based on a slow and controlled temperature drop in several steps. We considered the melting temperature (T_m) of each of the complementary fragments that must hybridize with each other to obtain the desired structure, avoiding the formation of other undesired ones.

The T_m of each fragment used in the synthesis of TDN was calculated by the expression $T_m = 64.9 + 41 \cdot (G + C - 16.4)/L$ [41], where G and C are the numbers of guanine and cytosine bases, respectively, in the DNA sequence and L is the total number of bases (17 bases). Considering the resulting T_m, the procedure of TDN synthesis described in the material and methods section was proposed.

To corroborate the efficacy of the proposed synthesis method, we characterized the structures formed by electrophoretic analysis, cryogenic electron microscopy (cryo-EM), optical microscopy (bright field and fluorescence), AFM, and dynamic light scattering (DLS).

Fig. 2B shows the obtained gel electrophoresis. As can be seen, TDN-ORF (lane 5) moved more slowly than either each single-stranded DNA oligonucleotide (Tetra-A-ORF, Tetra-B, Tetra-C and Tetra-D, respectively, in lanes 1 to 4) or any trimer combination lacking one strand (TDN-ORF without Tetra-A-ORF, Tetra-B, Tetra-C or Tetra-D, respectively, in lanes 6 to 9). These results point out a successful synthesis of the TDN-ORF [16] and agree well with the cryo-EM images of TDN (Fig. 2C).

Bright-field and fluorescence images of the TDN were carried out using FAM labeled TDN-ORF (TDN-ORF-FAM), synthesized by using a Tetra-A sequence carrying the ORF1ab gene capture probe and the fluorophore FAM (Tetra-A-ORF-FAM; see Table S1). The images of TDN-
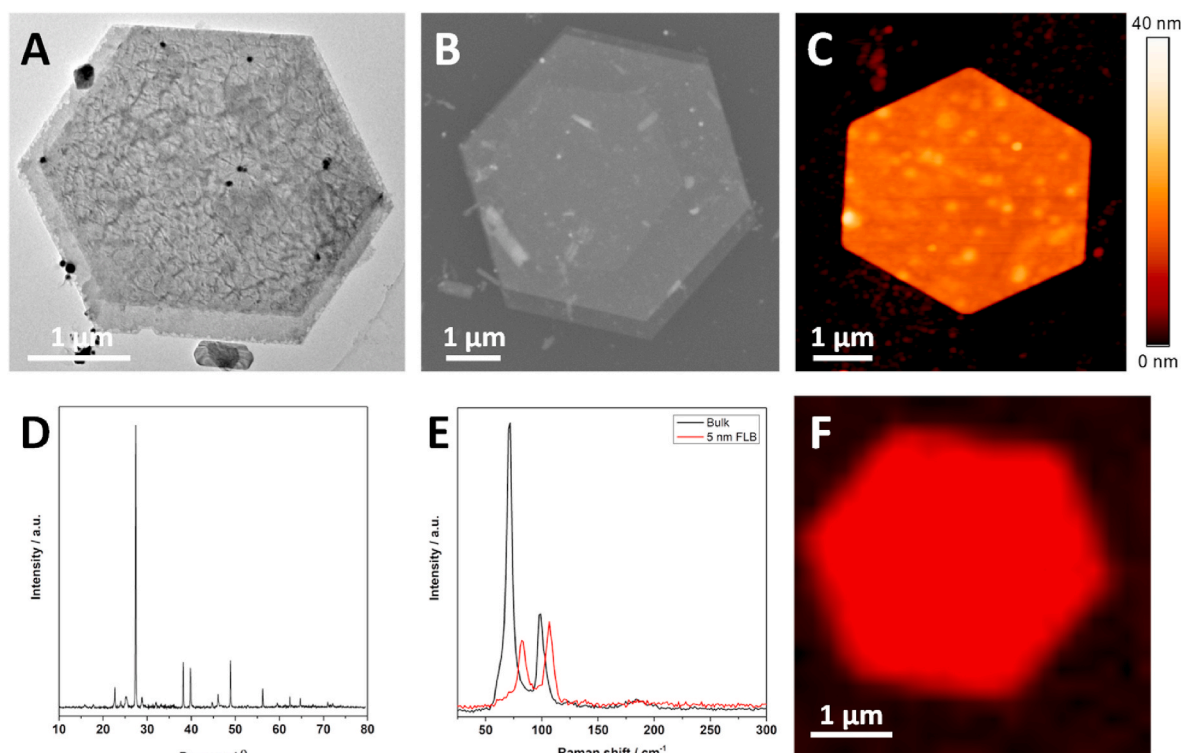
Fig. 1. (A) TEM and (B) SEM image of a representative FLB hexagon. (C) AFM image of a representative FLB hexagon with a thickness of 10 nm. Color scale bar of the height. (D) XRPD spectrum of the isolated FLB hexagons. (E) Raman spectra of bulk (black line) and an FLB hexagon of 5 nm thick (red line). (F) Raman mapping of an FLB hexagon.
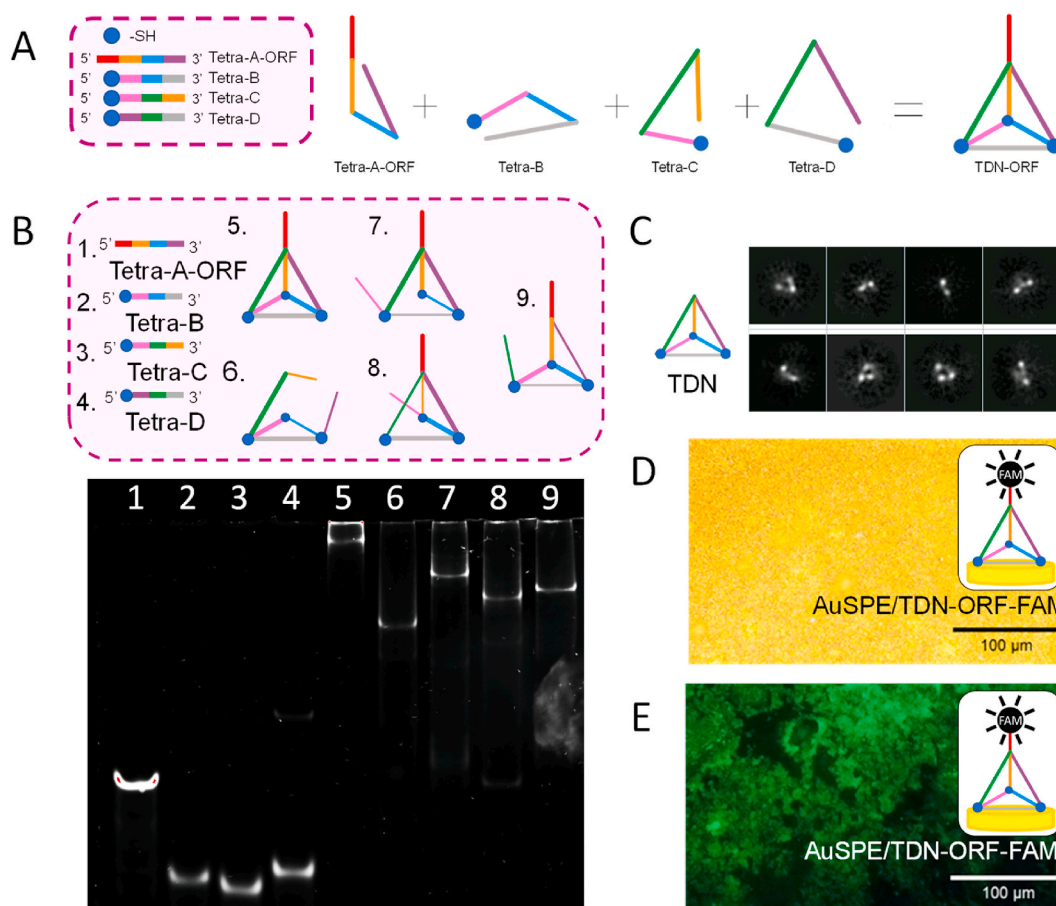
Fig. 2. (A) TDN-ORF design. Red line represents the SARS-CoV-2 ORF1ab gene capture probe. (B) Gel electrophoresis analysis of the TDN-ORF synthesis and schematic representation of the sample analyzed in each lane: lanes 1 to 4 stand for control experiment for single-stranded DNA oligonucleotides (Tetra-A-ORF, Tetra-B, Tetra-C and Tetra-D, respectively); lane 5 represents TDN-ORF; lanes 6 to 9 stands for a trimer combination lacking one strand (Tetra-A-ORF, Tetra-B, Tetra-C or Tetra-D, respectively). (C) TDN cryo-EM images. AuSPE/TDN-ORF-FAM images obtained by (D) bright field and (E) fluorescence optical microscopy.

ORF-FAM on gold screen-printed electrodes are presented in Fig. 2D and E. As can be seen, the fluorescence corresponding to the FAM molecule attached to the TDN is observed (Fig. 2E), confirming their successful synthesis and anchoring on the gold surface.

Individual TDN-ORF have also been imaged in non-contact mode AFM (Fig. S6), on recently cleaved mica (Figs. S6A and S6C) and on Au (111) flame annealed surface (Figs. S6B and S6D). Averaged height measured on more than 20 profiles is 8 ± 1 nm and 7 ± 2 nm, on mica and gold, respectively. Recently cleaved mica has a cleaner surface than gold which is the reason why the individual TDN-ORF shows less height on gold. Since the TDN-ORF are smaller than the tip size ($\sim$20 nm), the width of the features in the profiles corresponds to the width of the tip.

Finally, zeta potential of TDN-ORF was evaluated by DLS. As expected, TDN-ORF have a negative surface charge with a single peak at -22 ± 2 mV, due to the phosphate backbone of nucleotides.

3.4. Biosensor development

The biosensor was developed following Scheme 1. In order to obtain reproducible results each step was characterized to confirm successful preparation of the biosensor, and several potential issues were carefully checked. A common issue of enzyme-labeled DNA sensors is the strong non-specific adsorption of the enzyme onto the transductor surface, even in the absence of DNA analyte, which may result in a high background and poor signal-to-noise ratio [42]. To know if this is the case in our system, we recorded the ECL signal obtained with different electrochemical platforms (AuSPE, CSPE, CSPE/FLB, GPHSPE, GPHSPE/FLB)

when they were exposed to Av-GOx, rinsed with water, and incubated with glucose before measuring their ECL signal in the presence of luminol. Although all platforms presented non-specific adsorption of the enzyme, CSPE/FLB showed the lowest signal (Fig. S7) and, therefore, was selected for further studies.

As previously mentioned, most DNA biosensors reported in the literature are based on the classical two-step assembly strategy, chemisorption of a thiolated single-stranded DNA probe followed by passivation with an alkanethiol such as mercaptohexanol (MCH) or 2-[2-(1-mercaptoundec-11-yloxy)-ethoxy]-ethanol (OEG) [16]. However, 3D DNA nanostructures have emerged as a novel proposal to enhance the recognition event between the probe and the analyte [37,43] even if probe immobilization is performed directly without the passivation step. Therefore, in the present work we have chosen this strategy, and the capture probe is at the vertex of a tetrahedral DNA nanostructure with three thiol groups at the basal vertices to allow the immobilization on the FLB.

We have compared the response of the biosensor prepared with the TDN-ORF developed or with a thiolated single-stranded ORF1ab capture probe (ORF-SH) towards 10 pM ORF-C. Consequently, three different biosensing platforms were developed: I) CSPE/FLB/ORF-SH, II) (CSPE/FLB/ORF-SH/OEG), and III) CSPE/FLB/TDN-ORF. The ECL signals of the three platforms, calculated by subtracting the blank (signal obtained without the analyte) from the biosensor response, of the three platforms were recorded (Fig. S8). The CSPE/FLB/TDN-ORF platform presents the highest response. These results confirm that the use of TDNs as probe carriers leads to an improved response of the final

biosensing platform than that obtained with a single-stranded probe, even using the classical two-step assembly strategy for the single-stranded probe immobilization.

We performed a morphological characterization by SEM with energy dispersive X-ray spectroscopy (EDX), bright field and fluorescence, X-ray photoelectron spectroscopy (XPS), Raman and ECL, of the different steps followed in the biosensor development with the aim of corroborating its successful fabrication.

Fig. 3 shows the SEM images of CSPE (Fig. 3A and D) and CSPE/FLB (Fig. 3B, C, 3E, and 3F). The secondary electrons (SE) images (Fig. 3A, B, and 3C) revealed topographic characteristics. In the backscattered electrons (BSE) images (Fig. 3D and E), different contrast areas corresponding to different materials (the whiter, the higher the atomic number) are observed. While the BSE image of CSPE did not show any contrast (Fig. 3D), implying the presence of just one type of material (carbon), in the image of CSPE/FLB (Fig. 3E), whiter areas corresponding to zones of higher atomic number material are observed. These lighter color areas correspond to bismuth, as the EDX spectra confirmed (Fig. 3F), proving the presence of FLB.

As depicted in Scheme 1, the second step is the immobilization of the tetrahedral DNA nanostructures, which carry ORF1ab gene capture probe (TDN-ORF) onto FLB by direct adsorption. We have performed optical microscopy (bright field and fluorescence) studies to assess the successful completion of this step. For these studies, instead of the TDN-ORF used in the biosensor development, the FAM labeled TDN-ORF (TDN-ORF-FAM) was again used. Fig. 3 shows optical microscopy images of bright field (Fig. 3G, H and 3I) and fluorescence (Fig. 3J, K and 3L) of CSPE (Fig. 3G and J), CSPE/FLB (Fig. 3H and K) and CSPE/FLB/TDN-ORF-FAM (Fig. 3I and L). As expected, only the CSPE/FLB/TDN-ORF-FAM shows fluorescence (Fig. 3L), due to the presence of TDN-ORF-FAM. This result confirms that the TDN-ORF is immobilized on the FLB.

Fig. 3 shows XPS (Fig. 3M, 3N and 3O) performed on the bare CSPE electrode (black dots), CSPE/FLB (red dots) and CSPE/FLB/TDN-ORF (blue dots). The presence of Bi species is shown in Fig. 3M, where up to three different chemical states of Bi are observed: Bi_2O_3 (the expected Bi oxide, with the 4 $f_{7/2}$ centered at 159.1 eV), BiOCl (centered at 160.5 eV) and a compound of Bi^{5+} with some H_2O or Bi acetate, that is not present when the DNA is attached (located at 162.1 eV). The evidence of the DNA anchoring on the FLB is shown by the N 1s (blue data in Fig. 3N) and P 2p (blue data in Fig. 3O) *core levels*. Due to the low amount of S from the thiol group, its low sensitivity (1.68 for S 2p while for the Bi 4f is 24.8) and the overlapping with the Bi peaks, it is not possible to discriminate between them and assess the presence of S in these samples.

Raman spectroscopy was also used for the biosensor characterization. As portrayed in Fig. S9, CSPE Raman spectrum (black curve) shows the characteristic D and G bands of carbon at 1343 and 1576 cm^{-1}, respectively. In addition, a mild signal is observed at approximately 2680 cm^{-1}, which corresponds to the D band overtone (G' band) [44]. After CSPE modification with FLB (CSPE/FLB; red curve) the characteristic signals for FLB hexagons are clear (the two active modes in Raman spectroscopy E_g and A_{1g}) as described above. Finally, the spectrum corresponding to the electrode modified with TDN-ORF (CSPE/FLB/TDN-ORF; blue curve) shows signals at 392, 801 and 1052 cm^{-1} that correspond to vibrations of the DNA phosphate backbone. Besides that, signals at 516, 599, 761, and 1151 cm^{-1} correspond to active Raman modes for adenine, guanine, cytosine, and thymine, respectively [45]. Based on the obtained results, it can be concluded that the electrode modification with FLB and the anchoring of TDN-ORF were developed successfully.

To confirm the utility of the developed ECL biosensor, the ECL signal of the platforms after each preparation step was measured. As can be seen in Fig. 4A, after incubation with glucose (step 6) and measurement of the ECL signal in the presence of luminol (step 7), only the final platform (CSPE/FLB/TDN-ORF/ORF-C/ORF-2-Biotin/Av-GOx) provides an ECL signal (purple curve). No signal is observed for the resulting platforms at the previous development steps, as we expected.

Finally, once the different steps followed in the biosensor development were characterized, the factors that have a great influence on its final response were optimized. Hence, the effect of FLB drop-casted on the electrode surface, Av-GOx concentration, Av-GOx exposure time and TDN-ORF concentration were studied (Fig. S10). The best results were obtained using 10.0 μL of FLB and 25.0 μg/mL of Av-GOx, a time of Av-GOx immobilization of 35 min, and a TDN-ORF concentration of 1.00 μM.

3.4.1. Biosensor response

The detection of the ORF1ab gene SARS-CoV-2 was carried out by measuring the biocatalyzed ECL signal under the optimal experimental conditions (see previous section). The CSPE/FLB/TDN-ORF platform was incubated with 10.0 μL of different concentrations of the analyte (100 aM, 1.00 fM, 10.0 fM, 100 fM, 1.00 pM, 10.0 pM, 100 pM, 1.00 nM, 100 nM and 1.00 μM). The biocatalyzed ECL response was measured using luminol as luminophore and in-situ generated hydrogen peroxide. As observed in Fig. 4B, a linear relationship between the registered ECL signal and the logarithm of analyte (ORF-C) concentration was found (ECL = 94 + 14.0 · log [ORF-C]; R = 0.99097). Values were obtained in terms of reproducibility from the mean and the standard deviation of three different biosensors prepared in the same manner. The percentage coefficient of variation (CV(%)) was calculated using the errors obtained in the calibration plot for each concentration. The range of CV(%) was found to be 3 % (for 1.00 fM) to 18 % (for 100 pM). Since sensitivity is defined as the rate of change of the signal to the corresponding change in analyte concentration and is equivalent to the slope of the calibration plot, in this case, it takes a value of 14.0 a.u. log(aM^{-1}). The limit of detection (LOD) and quantification (LOQ) were estimated according to the 3·Sb·m^{-1} and 10·Sb·m^{-1} criteria, respectively, where Sb is the standard deviation of the blank signal (signal obtained incubating with PBS without the analyte) and m is the slope of the calibration plot. LOD and LOQ were of 4.31 aM and 14.4 aM, respectively.

The selectivity of the biosensor was also evaluated. The biosensor response to different samples containing 10.0 pM ORF-C in the absence and presence of the same concentration potential interferents, including other virus sequences as SARS-CoV-1 and Influenza A (H7N9), and a non-complementary DNA sequence (ORF-NC) was recorded. As can be observed in Fig. 4C, the response is quite similar, even in the presence of potential interferents. These results indicate that the biosensor can detect a specific sequence from SARS-CoV-2 genome even while being exposed to potential interfering sequences.

The stability of the biosensor was also evaluated by measuring the biosensor response of different devices prepared at the same time and stored at 4 °C over time. The results showed that the initial recognition signal was kept after 55 days (Fig. S11).

3.4.2. SARS-CoV-2 ORF1ab gene direct detection in nasopharyngeal samples

The applicability of the biosensor was evaluated by directly measuring its response to the SARS-CoV-2 RNA extracted from nasopharyngeal samples of COVID-19 patients, avoiding any amplification process such as PCR (see 1.1.2. of SI). The samples were provided and previously analyzed by RT-qPCR at Hospital Ramon y Cajal to validate the results obtained with the biosensor. Three nasopharyngeal samples from infected patients with different viral load (15, 20 and 29 Cts) and five negative samples from non-infected patients, used as control, were treated as described in detail in the SI and further analyzed using the developed ECL biosensor. Fig. 4D shows the biosensor responses to all analyzed samples. As can be observed, the responses of the two infected patients with the higher viral loads (P2 (Cts 20) and P3 (Cts 15)) are clearly greater than that of the non-infected patient. However, in the case of the infected patient with low viral load (P1 (Cts 29)) the response is quite similar to the non-infected one. The statistical analysis confirms that the biosensor responses to P2 (Cts 20) and P3 (Cts 15) are
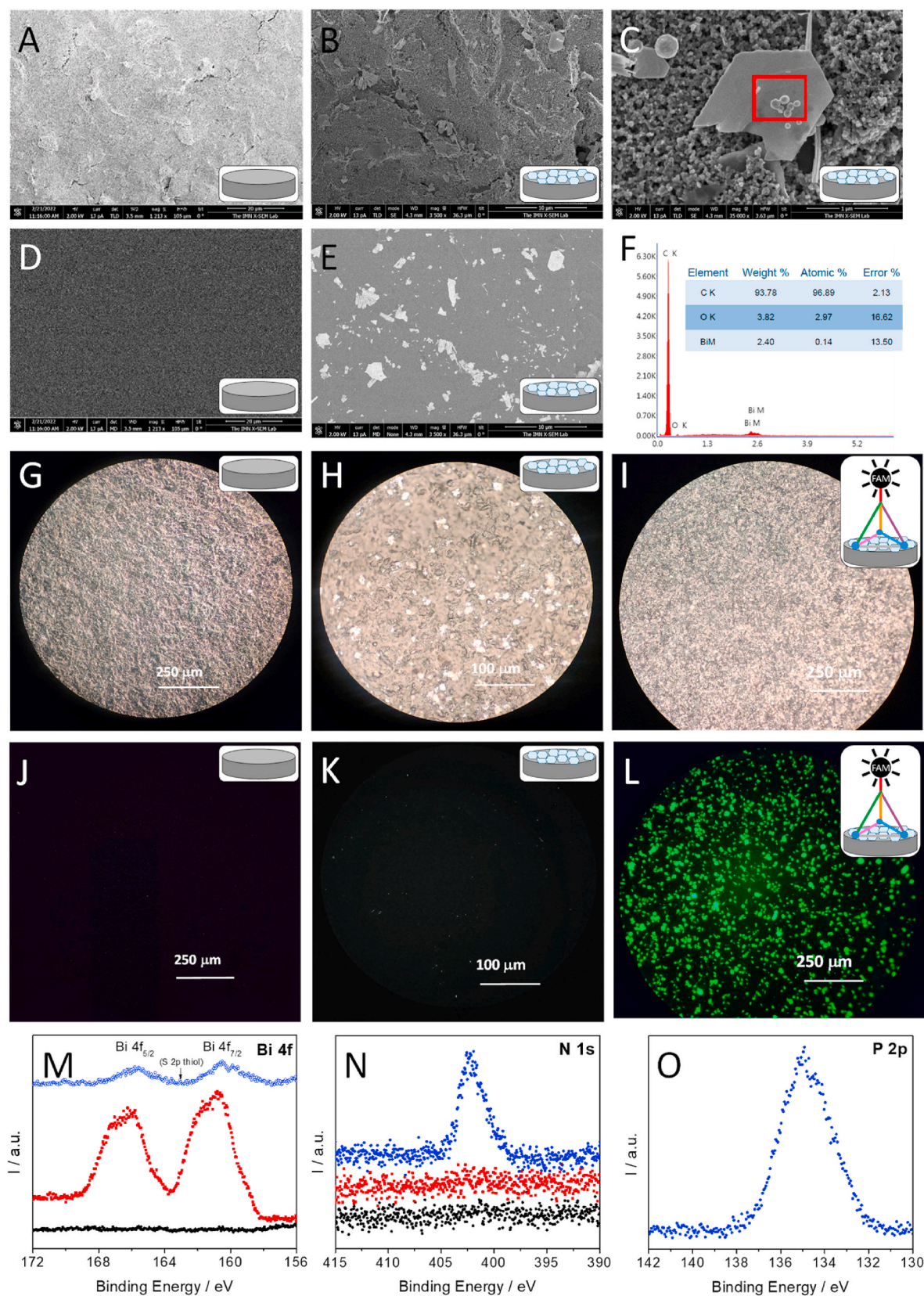
Fig. 3. (A, B and C) Secondary and (D and E) backscattered electrons SEM images of (A and D) CSPE and (B, C and E) CSPE/FLB. (F) EDX spectra on the CSPE/FLB area marked on Fig. 3C (20 kV, live time: 50 s, resolution: 129.3 eV). (G, H and I) Bright field and (J, K and L) fluorescence optical microscopy images of (G and J) CSPE, (H and K) CSPE/FLB and (I and L) CSPE/FLB/TDN-ORF-FAM. XPS *core levels* of (M) Bi 4f, (N) N 1s and (O) P 2p for the bare CSPE (black dots), CSPE/FLB (red dots) and CSPE/FLB/TDN-ORF (blue dots).
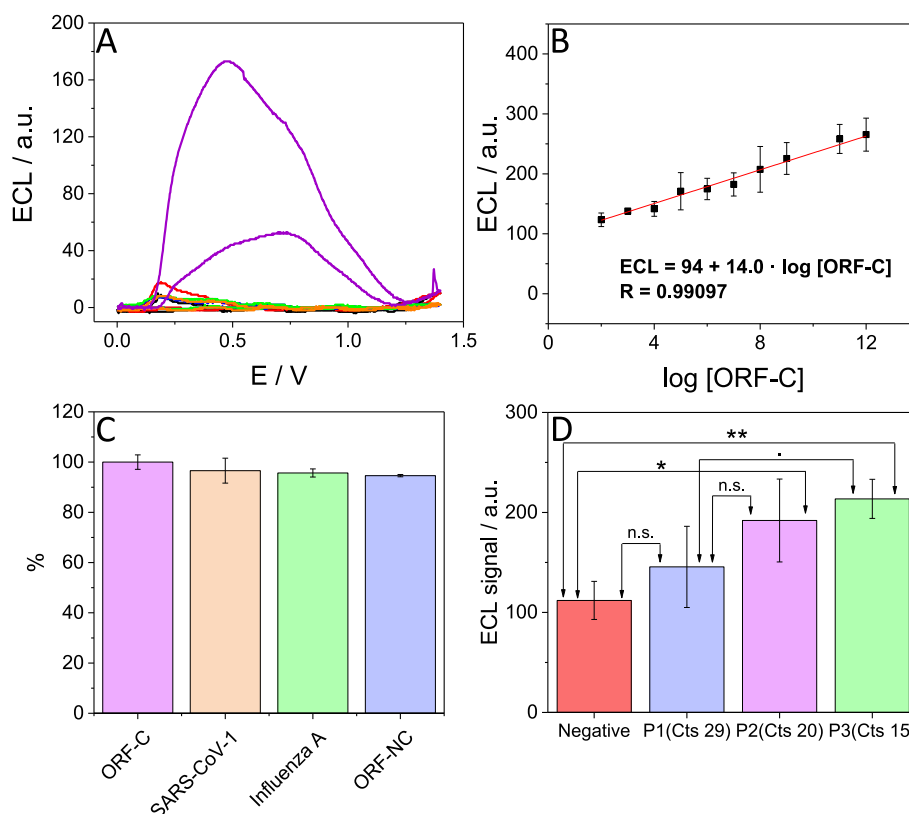
Fig. 4. (A) ECL biosensor response at the different development steps after incubation with 25.0 μL of 30 mM glucose and further addition of luminol up to 50 μM: CSPE (black curve), CSPE/FLB (red curve), CSPE/FLB/TDN-ORF (blue curve), CSPE/FLB/TDN-ORF/ORF-C (green curve), CSPE/FLB/TDN-ORF/ORF-C/ORF-2-Biotin (orange curve) and CSPE/FLB/TDN-ORF/ORF-C/ORF-2-Biotin/Av-GOx (purple curve). ECL signal was generated by applying a cyclic potential scan from 0.00 V to 1.40 V at a scan rate of 100 mV/s. (B) Calibration curve of the ECL biosensor response versus the logarithm of ORF-C (from 100 aM to 1.00 μM). (C) ECL biosensor response to ORF-C in the absence (purple bar) or in the presence of SARS-CoV-1 (pink bar), Influenza A (green bar), and non-complementary SARS-CoV-2 DNA sequence (blue bar). (D) Biosensor response to nasopharyngeal samples of negative SARS-CoV-2 patients (mean of 5 negatives) and infected patients (Patient 1 (P1; Cts 29), patient 2 (P2; Cts 20) and patient 3 (P3; Cts 15)). Data are presented as mean ± SD (n = 3 for positive samples and n = 5 for negative samples) in terms of ECL signal. Statistical analysis was performed using one-way ANOVA with Tukey's test (pairwise comparison). Signif. Codes: 0 '***' 0.001 '**' 0.01 '*' 0.05 '.' 0.1 '1.

significantly different (significance level of 0.01 and 0.001, respectively) to the non-infected patient (negative), but there is no significant difference between the responses to the infected patient with low viral load (P1; Cts 29) and the control. From these results, it can be concluded that the biosensor can detect a SARS-CoV-2 sequence on human nasopharyngeal samples from infected patients in the case of viral loads equal to or higher than 20 Cts, avoiding any amplification process.

Compared to other ECL biosensors based on some amplification technique and other electrochemical (EQ) biosensors (Table S2), which detect SARS-CoV-2 genes, the biosensor described in this work, based on the combination of FLB and tetrahedral DNA nanostructures, has the lowest LOD with a wider linear range. In addition, this biosensor avoids any amplification step. In conclusion, this biosensor represents a promising alternative for the selective detection of the virus, which could be extrapolated to other diseases and useful for a better control of potential future pandemics.

4. Conclusions

The use of TDNs combined with FLB has been proven as a successful alternative strategy to design a new ECL DNA biosensor for the selective and sensitive diagnosis of COVID-19. FLB allows anchoring thiolated TDNs, while the designed TDN (carrying ORF1ab gene capture probe in one of its vertices (TDN-ORF)) permits the achievement of improved probe-DNA target recognition. The transduction is carried out by measuring a biocatalyzed ECL signal using the luminophore luminol and H_2O_2 as co-reactant, which was in-situ generated by the glucose oxidase immobilized on the biosensing platform. The biosensor can detect the specific sequence ORF1ab of SARS-CoV-2 genome with a detection limit of 4.31 aM, value that is lower than others achieved by biosensors previously described, even in the presence of other potential interferent sequences from other viruses or a non-complementary DNA sequence. Moreover, the applicability of the developed biosensor has been evaluated by detecting SARS-CoV-2 in nasopharyngeal samples from COVID-19 patients without the need for any amplification process.

Appendix A. Supplementary data

Supplementary data to this article can be found online at https://doi.org/10.1016/j.talanta.2023.125405.

References

[1] M.A. Zamzami, G. Rabbani, A. Ahmad, A.A. Basalah, W.H. Al-Sabban, S. Nate Ahn, H. Choudhry, Carbon nanotube field-effect transistor (CNT-FET)-based biosensor for rapid detection of SARS-CoV-2 (COVID-19) surface spike protein S1, Bioelectrochemistry 143 (2022), https://doi.org/10.1016/J.BIOELECHEM.2021.107982.

[2] J.C. Abrego-Martinez, M. Jafari, S. Chergui, C. Pavel, D. Che, M. Siaj, Aptamer-based electrochemical biosensor for rapid detection of SARS-CoV-2: nanoscale electrode-aptamer-SARS-CoV-2 imaging by photo-induced force microscopy, Biosens. Bioelectron. 195 (2022), 113595, https://doi.org/10.1016/J.BIOS.2021.113595.

[3] D.S. Chauhan, R. Prasad, R. Srivastava, M. Jaggi, S.C. Chauhan, M.M. Yallapu, Comprehensive review on current interventions, diagnostics, and nanotechnology perspectives against SARS-CoV-2, Bioconjugate Chem. 31 (2020) 2021–2045.

[4] N. Kumar, N.P. Shetti, S. Jagannath, T.M. Aminabhavi, Electrochemical sensors for the detection of SARS-CoV-2 virus, Chem. Eng. J. 430 (2022), 132966, https://doi.org/10.1016/J.CEJ.2021.132966.

[5] J. Zeng, P.A. Duarte, Y. Ma, O. Savchenko, L. Shoute, Y. Khaniani, S. Babiuk, R. Zhuo, G.N. Abdelrasoul, C. Charlton, J.N. Kanji, L. Babiuk, C. Edward, J. Chen, An impedimetric biosensor for COVID-19 serology test and modification of sensor performance via dielectrophoresis force, Biosens. Bioelectron. 213 (2022), 114476, https://doi.org/10.1016/J.BIOS.2022.114476.

[6] L. Ma, L. Yin, X. Li, S. Chen, L. Peng, G. Liu, S. Ye, W. Zhang, S. Man, A smartphone-based visual biosensor for CRISPR-Cas powered SARS-CoV-2 diagnostics, Biosens. Bioelectron. 195 (2022), 113646, https://doi.org/10.1016/J.BIOS.2021.113646.

[7] Y. Peng, Y. Pan, Z. Sun, J. Li, Y. Yi, J. Yang, G. Li, An electrochemical biosensor for sensitive analysis of the SARS-CoV-2 RNA, Biosens. Bioelectron. 186 (2021), 113309, https://doi.org/10.1016/J.BIOS.2021.113309.

[8] S. Suleman, S.K. Shukla, N. Malhotra, S.D. Bukkitgar, N.P. Shetti, R. Pilloton, J. Narang, Y. Nee Tan, T.M. Aminabhavi, Point of care detection of COVID-19: advancement in biosensing and diagnostic methods, Chem. Eng. J. 414 (2021), 128759, https://doi.org/10.1016/J.CEJ.2021.128759.

[9] M. Garg, A.L. Sharma, S. Singh, Advancement in biosensors for inflammatory biomarkers of SARS-CoV-2 during 2019–2020, Biosens. Bioelectron. 171 (2021), 112703, https://doi.org/10.1016/J.BIOS.2020.112703.

[10] Y. Deng, Y. Peng, L. Wang, M. Wang, T. Zhou, L. Xiang, J. Li, J. Yang, G. Li, Target-triggered cascade signal amplification for sensitive electrochemical detection of SARS-CoV-2 with clinical application, Anal. Chim. Acta 1208 (2022), 339846, https://doi.org/10.1016/J.ACA.2022.339846.

[11] Z. Fan, B. Yao, Y. Ding, J. Zhao, M. Xie, K. Zhang, Entropy-driven amplified electrochemiluminescence biosensor for RdRp gene of SARS-CoV-2 detection with self-assembled DNA tetrahedron scaffolds, Biosens. Bioelectron. 178 (2021), https://doi.org/10.1016/J.BIOS.2021.113015.

[12] T. Yin, Y. Ye, W. Dong, G. Jie, Electrochemiluminescence resonance energy transfer biosensing platform between g-C3N4 nanosheet and Ru–SiO2@FA for dual-wavelength ratiometric detection of SARS-CoV-2 RdRp gene, Biosens. Bioelectron. 215 (2022), 114580, https://doi.org/10.1016/J.BIOS.2022.114580.

[13] C. Jiang, X. Mu, S. Liu, Z. Liu, B. Du, J. Wang, J. Xu, A study of the detection of SARS-CoV-2 ORF1ab gene by the use of electrochemiluminescent biosensor based on dual-probe hybridization, Sensors 22 (2022) 2402, https://doi.org/10.3390/S22062402.

[14] K. Zhang, Z. Fan, Y. Huang, Y. Ding, M. Xie, M. Wang, Hybridization chain reaction circuit-based electrochemiluminescent biosensor for SARS-cov-2 RdRp gene assay, Talanta 240 (2022), 123207, https://doi.org/10.1016/J.TALANTA.2022.123207.

[15] L. Gutiérrez-Gálvez, R. del Caño, I. Menéndez-Luque, D. García-Nieto, M. Rodríguez-Peña, M. Luna, T. Pineda, F. Pariente, T. García-Mendiola, E. Lorenzo, Electrochemiluminescent nanostructured DNA biosensor for SARS-CoV-2 detection, Talanta 240 (2022), 123203, https://doi.org/10.1016/J.TALANTA.2021.123203.

[16] H. Pei, N. Lu, Y. Wen, S. Song, Y. Liu, H. Yan, C. Fan, A DNA nanostructure-based biomolecular probe carrier platform for electrochemical biosensing, Adv. Mater. 22 (2010) 4754–4758, https://doi.org/10.1002/adma.201002767.

[17] Y. Wen, H. Pei, Y. Shen, J. Xi, M. Lin, N. Lu, X. Shen, J. Li, C. Fan, DNA Nanostructure-based Interfacial engineering for PCR-free ultrasensitive electrochemical analysis of microRNA, Sci. Rep. 2 (2012), https://doi.org/10.1038/srep00867.

[18] H. Li, K. Zhang, F. Pi, S. Guo, L. Shlyakhtenko, W. Chiu, D. Shu, P. Guo, H. Li, F. Pi, S. Guo, D. Shu, P. Guo, K. Zhang, W. Chiu Verna, M. McLean, L. Shlyakhtenko, Controllable self-assembly of RNA tetrahedrons with precise shape and size for cancer targeting, Adv. Mater. 28 (2016) 7501–7507, https://doi.org/10.1002/ADMA.201601976.

[19] Z. Fan, B. Yao, Y. Ding, D. Xu, J. Zhao, K. Zhang, Rational engineering the DNA tetrahedrons of dual wavelength ratiometric electrochemiluminescence biosensor for high efficient detection of SARS-CoV-2 RdRp gene by using entropy-driven and bipedal DNA walker amplification strategy, Chem. Eng. J. 427 (2022), https://doi.org/10.1016/J.CEJ.2021.131686.

[20] C.C. Mayorga-Martinez, R. Gusmão, Z. Sofer, M. Pumera, Pnictogen-based enzymatic phenol biosensors: phosphorene, arsenene, antimonene, and bismuthene, Angew. Chem. Int. Ed. 58 (2019) 134–138, https://doi.org/10.1002/ANIE.201808846.

[21] M.S. Ozer, Z. Eroglu, A.S. Yalin, M. Kılıç, U. Rothlisberger, O. Metin, Bismuthene as a versatile photocatalyst operating under variable conditions for the photoredox CH bond functionalization, Appl. Catal., B 304 (2022), 120957, https://doi.org/10.1016/J.APCATB.2021.120957.

[22] T. Xue, S.R. Bongu, H. Huang, W. Liang, Y. Wang, F. Zhang, Z. Liu, Y. Zhang, H. Zhang, X. Cui, Ultrasensitive detection of microRNA using a bismuthene-enabled fluorescence quenching biosensor, Chem. Commun. 56 (2020) 7041–7044, https://doi.org/10.1039/D0CC01004A.

[23] I. Torres, A.M. Villa-Manso, M. Revenga-Parra, C. Gutiérrez-Sánchez, D.A. Aldave, E. Salagre, E.G. Michel, M. Varela, J. Gómez-Herrero, E. Lorenzo, F. Pariente, F. Zamora, Preparation of high-quality few-layers bismuthene hexagons, Appl. Mater. Today 26 (2022), 101360, https://doi.org/10.1016/J.APMT.2021.101360.

[24] M.A. Tapia, C. Pérez-Ràfols, R. Gusmão, N. Serrano, Z. Sofer, J.M. Díaz-Cruz, Enhanced voltammetric determination of metal ions by using a bismuthene-modified screen-printed electrode, Electrochim. Acta 362 (2020), 137144, https://doi.org/10.1016/J.ELECTACTA.2020.137144.

[25] A.C. Lazanas, K. Tsirka, A.S. Paipetis, M.I. Prodromidis, 2D bismuthene/graphene modified electrodes for the ultra-sensitive stripping voltammetric determination of lead and cadmium, Electrochim. Acta 336 (2020), 135726, https://doi.org/10.1016/J.ELECTACTA.2020.135726.

[26] S. Alwarappan, N. Nesakumar, D. Sun, T.Y. Hu, C.Z. Li, 2D metal carbides and nitrides (MXenes) for sensors and biosensors, Biosens. Bioelectron. 205 (2022), https://doi.org/10.1016/j.bios.2021.113943.

[27] M. Adamovski, A. Zajac, P. Gründler, G.U. Flechsig, Self-assembled monolayers on bismuth electrodes, Electrochem. Commun. 8 (2006) 932–936, https://doi.org/10.1016/J.ELECOM.2006.03.031.

[28] T. Romann, V. Grozovski, E. Lust, Formation of the bismuth thiolate compound layer on bismuth surface, Electrochem. Commun. 9 (2007) 2507–2513, https://doi.org/10.1016/J.ELECOM.2007.07.029.

[29] N. Yu, Z. Wang, J. Zhang, Z. Liu, B. Zhu, J. Yu, M. Zhu, C. Peng, Z. Chen, Thiol-capped Bi nanoparticles as stable and all-in-one type theranostic nanoagents for tumor imaging and thermoradiotherapy, Biomaterials 161 (2018) 279–291, https://doi.org/10.1016/J.BIOMATERIALS.2018.01.047.

[30] G. Alessio Verni, B. Long, F. Gity, M. Lanius, P. Schüffelgen, G. Mussler, D. Grützmacher, J. Greer, J.D. Holmes, Oxide removal and stabilization of bismuth thin films through chemically bound thiol layers, RSC Adv. 8 (2018) 33368–33373, https://doi.org/10.1039/C8RA06840B.

[31] T. Sun, J. Du, Z. Li, F. Zhao, Recent Advancement in the development of hybridization chain reaction-based electrochemiluminescence biosensors, Int. J. Electrochem. Sci. 17 (2022), 220650, https://doi.org/10.20964/2022.06.35.

[32] Y. Huang, Y. Yao, Y. Wang, L. Chen, Y. Zeng, L. Li, L. Guo, Strategies for enhancing the sensitivity of electrochemiluminescence biosensors, Biosensors 12 (2022) 750, https://doi.org/10.3390/BIOS12090750.

[33] J.A. Steele, R.A. Lewis, In situ micro-Raman studies of laser-induced bismuth oxidation reveals metastability of β-Bi2O3 microislands, Opt. Mater. Express 4 (10) (2014) 2133–2142, https://doi.org/10.1364/OME.4.002133, 2133–2142.

[34] I. Torres, M. Alcaraz, R. Sanchis-Gual, J.A. Carrasco, M. Fickert, M. Assebban, C. Gibaja, J. Dolle, D.A. Aldave, C. Gómez-Navarro, E. Salagre, E. García Michel, M. Varela, J. Gómez-Herrero, G. Abellán, F. Zamora, Continuous-flow synthesis of high-quality few-layer antimonene hexagons, Adv. Funct. Mater. 31 (2021), 2101616, https://doi.org/10.1002/ADFM.202101616.

[35] C. Gibaja, D. Rodriguez-San-Miguel, P. Ares, J. ulio Gómez-Herrero, M. Varela, R. Gillen, J. Maultzsch, F. Hauke, A. Hirsch, G. Abellμn, Fø Zamora, C. Gibaja,

D. Rodriguez-San-Miguel, D. Zamora, P. Ares, J. Gómez-Herrero, D. Gillen, J. Maultzsch, D.H. auke, A. Hirsch, Few-layer antimonene by liquid-phase exfoliation, Angew. Chem. Int. Ed. 55 (2016) 14345–14349, https://doi.org/10.1002/ANIE.201605298.

[36] Z. Li, B. Zhao, D. Wang, Y. Wen, G. Liu, H. Dong, S. Song, C. Fan, DNA nanostructure-based universal microarray platform for high-efficiency multiplex bioanalysis in biofluids, ACS Appl. Mater. Interfaces 6 (2014) 17944–17953, https://doi.org/10.1021/am5047735.

[37] H. Pei, N. Lu, Y. Wen, S. Song, Y. Liu, H. Yan, C. Fan, A DNA nanostructure-based biomolecular probe carrier platform for electrochemical biosensing, Adv. Mater. 22 (2010) 4754–4758, https://doi.org/10.1002/ADMA.201002767.

[38] Y. Wen, H. Pei, Y. Wan, Y. Su, Q. Huang, S. Song, C. Fan, DNA nanostructure-decorated surfaces for enhanced aptamer-target binding and electrochemical cocaine sensors, Anal. Chem. 83 (2011) 7418–7423, https://doi.org/10.1021/ac201491p.

[39] N. Mitchell, R. Schlapak, M. Kastner, D. Armitage, W. Chrzanowski, J. Riener, P. Hinterdorfer, A. Ebner, S. Howorka, A DNA nanostructure for the functional assembly of chemical groups with tunable stoichiometry and defined nanoscale geometry, Angew. Chem. Int. Ed. 48 (2009) 525–527, https://doi.org/10.1002/anie.200804264.

[40] Z. Ge, M. Lin, P. Wang, H. Pei, J. Yan, J. Shi, Q. Huang, D. He, C. Fan, X. Zuo, Hybridization chain reaction amplification of microRNA detection with a tetrahedral DNA nanostructure-based electrochemical biosensor, Anal. Chem. 86 (2014) 2124–2130, https://doi.org/10.1021/ac4037262.

[41] R. Kalendar, D. Lee, A.H. Schulman, FastPCR Software for PCR Primer and Probe Design and Repeat Search Complexity of Repeat Sequences in Differential Genomes of Plant/animal Infecting Viruses View Project PCR and qPCR Assays Development View Project, 2009. https://www.researchgate.net/publication/284652273.

[42] L. Zhang, D. Li, W. Meng, Q. Huang, Y. Su, L. Wang, S. Song, C. Fan, Sequence-specific DNA detection by using biocatalyzed electrochemiluminescence and non-fouling surfaces, Biosens. Bioelectron. 25 (2009) 368–372, https://doi.org/10.1016/J.BIOS.2009.07.019.

[43] H. Pei, Y. Wan, J. Li, H. Hu, Y. Su, Q. Huang, C. Fan, Regenerable electrochemical immunological sensing at DNA nanostructure-decorated gold surfaces, Chem. Commun. 47 (2011) 6254–6256, https://doi.org/10.1039/C1CC11660F.

[44] M.A. Pimenta, G. Dresselhaus, M.S. Dresselhaus, L.G. Cançado, A. Jorio, R. Saito, Studying disorder in graphite-based systems by Raman spectroscopy, Phys. Chem. Chem. Phys. 9 (2007) 1276–1290, https://doi.org/10.1039/B613962K.

[45] B. Prescott, W. Steinmetz, G.J. Thomas, Characterization of DNA structures by laser Raman spectroscopy, Biopolymers 23 (1984) 235–256, https://doi.org/10.1002/BIP.360230206.